




Fine cubic Cu₂O nanocrystals as highly selective catalyst for propylene epoxidation with molecular oxygen

Wei Xiong^{1,7}, Xiang-Kui Gu ^{2,7}, Zhenhua Zhang³, Peng Chai¹, Yijing Zang⁴, Zongyou Yu¹, Dan Li¹, Hui Zhang ⁴, Zhi Liu^{4,5} & Weixin Huang ^{1,6}✉

Propylene epoxidation with O₂ to propylene oxide is a very valuable reaction but remains as a long-standing challenge due to unavailable efficient catalysts with high selectivity. Herein, we successfully explore 27 nm-sized cubic Cu₂O nanocrystals enclosed with {100} faces and {110} edges as a highly selective catalyst for propylene epoxidation with O₂, which acquires propylene oxide selectivity of more than 80% at 90–110 °C. Propylene epoxidation with weakly-adsorbed O₂ species at the {110} edge sites exhibits a low barrier and is the dominant reaction occurring at low reaction temperatures, leading to the high propylene oxide selectivity. Such a weakly-adsorbed O₂ species is not stable at high reaction temperatures, and the surface lattice oxygen species becomes the active oxygen species to participate in propylene epoxidation to propylene oxide and propylene partial oxidation to acrolein at the {110} edge sites and propylene combustion to CO₂ at the {100} face sites, which all exhibit high barriers and result in decreased propylene oxide selectivity.

¹Hefei National Laboratory for Physical Sciences at the Microscale, Key Laboratory of Surface and Interface Chemistry and Energy Catalysis of Anhui Higher Education Institutes and Department of Chemical Physics, University of Science and Technology of China, 230026 Hefei, People's Republic of China. ²School of Power and Mechanical Engineering, Wuhan University, 430072 Wuhan, People's Republic of China. ³Key Laboratory of the Ministry of Education for Advanced Catalysis Materials, Zhejiang Key Laboratory for Reactive Chemistry on Solid Surfaces, Institute of Physical Chemistry, Zhejiang Normal University, 321004 Jinhua, People's Republic of China. ⁴State Key Laboratory of Functional Materials for Informatics, Shanghai Institute of Microsystem and Information Technology, Chinese Academy of Sciences, 200050 Shanghai, People's Republic of China. ⁵School of Physical Science and Technology, ShanghaiTech University, 201210 Shanghai, People's Republic of China. ⁶Dalian National Laboratory for Clean Energy, 116023 Dalian, People's Republic of China. ⁷These authors contributed equally: Wei Xiong, Xiang-Kui Gu. ✉email: huangwx@ustc.edu.cn

Propylene oxide (PO) is a platform chemical for numerous commodity chemicals¹, such as polyols and glycol ethers. The current industrial production of PO from propylene involves uses of chlorohydrin or H₂O₂ and is cost-ineffective and environment-unfriendly^{2,3}. Among various alternative technologies^{4–7}, propylene epoxidation with O₂ to PO is considered most economic and environment-friendly. However, it is meanwhile one of the most challenging catalytic reactions due to unavailable efficient catalysts with high selectivity^{8–12}. Cu-based catalysts have been widely studied as a promising catalyst^{13–18}, but the reported PO selectivity is not satisfying.

Fundamental understanding of active sites for heterogeneous catalytic reactions is an efficient approach to explore novel catalysts. Successful examples have been only a few and they are all based on density functional theory (DFT) calculations^{19–23}. Herein, we report a successful exploration of fine cubic Cu₂O nanocrystals (NCs) enclosed with {100} faces and {110} edges as a highly selective catalyst for propylene epoxidation with O₂ to PO, guided by an experimental fundamental understanding of the active site. We previously used large rhombic dodecahedral NCs (denoted as d-Cu₂O) enclosed with Cu₂O{110} facets to identify the Cu₂O{110} facets as the active facet for propylene epoxidation with O₂¹⁷, in which, however, reaction temperatures above 150 °C were adopted due to the low density of the active site on the used large d-Cu₂O NCs, favoring the combustion reaction and limiting the acquired PO selectivity. Later large d-Cu₂O NCs with the Cl[−] dopant were reported to exhibit enhanced activity in catalyzing propylene epoxidation with O₂ and consequently high PO selectivity at low temperatures⁹. Thus, a reasonable strategy to explore highly selective catalysts for propylene epoxidation with O₂ to PO is to synthesize uniform fine d-Cu₂O NCs with high densities of Cu₂O{110} active site, which, unfortunately, has not been realized. Meanwhile, Cu₂O cubes (denoted as c-Cu₂O) are enclosed with the {100} faces and {110} edges. We found that the densities of {110} edges are high on Cu₂O cubes (denoted as c-Cu₂O) finer than 100 nm and the {110} edge sites on these fine c-Cu₂O NCs, rather than the {100} face sites, are the dominant active site catalyzing the CO oxidation reaction²⁴. Intrigued by these findings, we have investigated propylene oxidation with O₂ over c-Cu₂O NCs with different sizes and report herein that fine c-Cu₂O NCs with an average size of 27 nm selectively catalyze propylene epoxidation with O₂ to PO at temperatures below 110 °C with the Cu₂O{110} edge sites as the active site. Interestingly, the reaction mechanism for PO production at the Cu₂O{110} active site was found to switch from weakly adsorbed O₂-participating Langmuir–Hinshelwood (LH) mechanism at low temperatures to surface lattice oxygen-participating Mars-van Krevelen (MvK) mechanism at high temperatures.

Results

Synthesis and structural characterizations catalysts. Following previously established procedures^{17,25–27}, uniform surfactant-free c-Cu₂O NCs with sizes of 27 ± 4.5, 106 ± 12, and 774 ± 147 nm were synthesized (Fig. 1a–c and Supplementary Fig. 1) and denoted as c-Cu₂O-27, c-Cu₂O-106, and c-Cu₂O-774, respectively. BET-specific surface areas of c-Cu₂O-27, c-Cu₂O-106, and c-Cu₂O-774 are 25.5, 11.2, and 1.5 m² g^{−1}, respectively. XPS spectra (Supplementary Fig. 2) show existences of only adventitious carbon and carbonates on the surfaces of various c-Cu₂O NCs. c-Cu₂O NCs are enclosed with O-terminated Cu₂O{100} faces and (Cu(I), O)-terminated Cu₂O{110} edges (Supplementary Fig. 3)^{24,28}. Based on the size distributions of various c-Cu₂O NCs, densities of Cu(110) edge sites and their fractions related to total surface Cu sites were estimated to be 6.44 × 10¹⁸/g_{Cu₂O} and 1.61% on c-Cu₂O-27, 4.08 × 10¹⁷/g_{Cu₂O}, and 0.42% on c-Cu₂O-

106, and 7.84 × 10¹⁵/g_{Cu₂O} and 0.06% on c-Cu₂O-774 (Supplementary Table 1), respectively. Surface sites of various Cu₂O NCs were probed by CO adsorption at 123 K with in-situ DRIFTS (Supplementary Fig. 4). Vibrational features of adsorbed CO were barely observed for c-Cu₂O-774 NCs, but a vibrational feature at 2109 cm^{−1} arising from CO adsorbed at the Cu(I) site²⁹ emerged for c-Cu₂O-106 NCs and grew greatly for c-Cu₂O-27 NCs. The Cu(I) sites for CO adsorption on c-Cu₂O NCs exist on the (Cu(I), O)-terminated Cu₂O{110} edges but not on the O-terminated Cu₂O{100} faces. Therefore, the density of Cu₂O{110} edges is too low on large c-Cu₂O-774 NCs to be probed by CO adsorption measured with DRIFTS, but becomes high enough on fine c-Cu₂O-106 and c-Cu₂O-27 NCs.

Catalytic performance in C₃H₆ oxidation with O₂. Various c-Cu₂O NCs exhibit size-dependent catalytic performance in propylene oxidation with O₂. As shown in Fig. 2 and Supplementary Fig. 5, c-Cu₂O-774 NCs became active at 190 °C and dominantly catalyzed propylene combustion to produce CO₂ with CO₂ selectivity above 80%. c-Cu₂O-27 and c-Cu₂O-106 NCs were much more active than c-Cu₂O-774 NCs, being catalytically active at 90 °C. Meanwhile, at comparable C₃H₆ conversions, c-Cu₂O-27 and c-Cu₂O-106 NCs exhibited much higher PO selectivities than c-Cu₂O-774 NCs. Strikingly, c-Cu₂O-27 and c-Cu₂O-106 NCs selectively catalyzed the propylene epoxidation with PO selectivity respectively of above 80 and 70% between 90 and 110 °C, but barely catalyzed propylene partial oxidation to acrolein. As the temperature increased above 110 °C, the CO₂ selectivity increased rapidly at the expense of PO selectivity, and the acrolein production emerged and grew.

The catalytic performance of c-Cu₂O-774 NCs is contributed by the Cu₂O{100} face sites that selectively catalyze the propylene combustion reaction¹⁷, while the very different catalytic performances of c-Cu₂O-27 and c-Cu₂O-106 NCs arise from both the Cu₂O{110} edge sites of enough high densities and the Cu₂O{100} face sites. The Cu₂O{110} facets were identified to selectively catalyze the propylene epoxidation reaction¹⁷. Therefore, the Cu₂O{110} edge sites of c-Cu₂O-27 and c-Cu₂O-106 NCs are the dominant surface sites catalyzing propylene oxidation between 90 and 110 °C, giving high PO selectivity, while the contribution from the Cu₂O{100} face sites increases with the reaction temperature, leading to increased CO₂ selectivity at the expense of PO selectivity. These results, on one hand, demonstrate that the Cu₂O{110} edge sites on c-Cu₂O-27 and c-Cu₂O-106 NCs are more active than the Cu₂O{100} face sites, on the other hand, demonstrates that the Cu₂O{110} site is active in selectively catalyzing the propylene epoxidation with O₂ at low temperatures. As far as we know, PO selectivity above 80% in propylene oxidation with O₂ catalyzed by c-Cu₂O-27 NCs are much higher than all previously reported Cu-based catalysts except the recently-reported Cl-doped d-Cu₂O NCs⁹. It is noteworthy that the catalytic selectivity of Cu₂O{110} edge sites of c-Cu₂O-27 and c-Cu₂O-106 NCs in catalyzing propylene oxidation with O₂ between 90 and 110 °C differs very much from that of Cu₂O{110} face sites of large d-Cu₂O NCs (d-Cu₂O-439) which became active only above 150 °C (Supplementary Fig. 6)¹⁷. In addition to the significantly higher PO selectivity over c-Cu₂O-27 and c-Cu₂O-106 NCs than over d-Cu₂O-439 NCs, acrolein was barely produced for c-Cu₂O-27 and c-Cu₂O-106 NCs but was a major product for d-Cu₂O-439 NCs. Thus the catalytic behavior of Cu₂O{110} sites in propylene oxidation with O₂ sensitively depends on the reaction temperature.

Structures of spent Cu₂O NCs after catalytic performance evaluations at different temperatures were characterized. Both microscopic (Fig. 1d, e and Supplementary Fig. 7) and

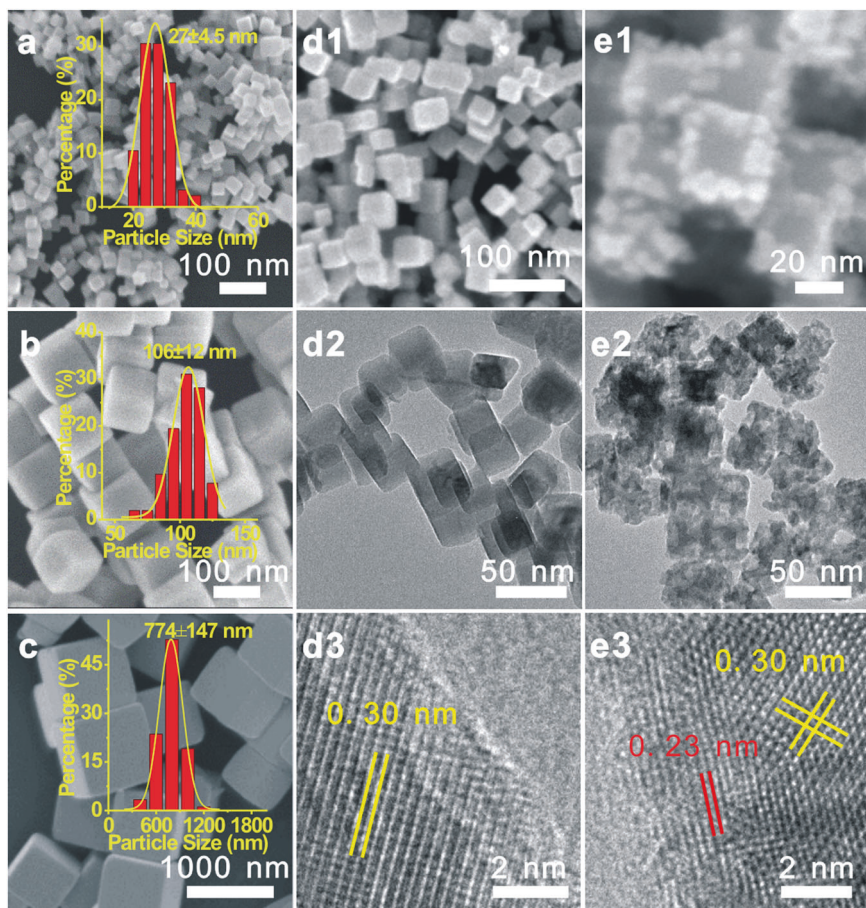


Fig. 1 Microscopic characterization of Cu_2O NCs. SEM images and particle size distributions of **a** $c\text{-Cu}_2\text{O-27}$, **b** $c\text{-Cu}_2\text{O-106}$, and **c** $c\text{-Cu}_2\text{O-774}$. SEM, TEM, and HRTEM images of $c\text{-Cu}_2\text{O-27}$ after evaluated in C_3H_6 oxidation with O_2 at 90 (**d1-d3**) and 150 °C (**e1-e3**). Lattice fringes of 0.30 and 0.23 nm correspond to the spacing of the $\text{Cu}_2\text{O}\{110\}$ (JCPDS card no. 78-2076) and $\text{CuO}\{111\}$ (JCPDS card no. 89-5899) crystal planes, respectively.

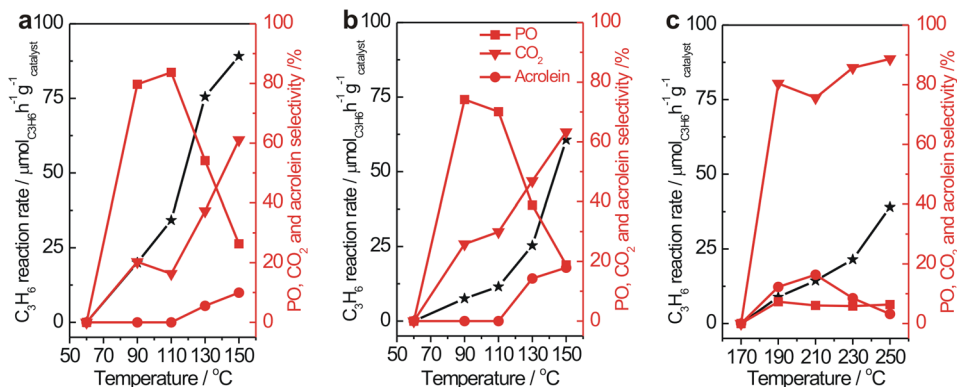


Fig. 2 Catalytic performance in C_3H_6 oxidation with O_2 . C_3H_6 reaction rate (black) and propylene oxide (PO), acrolein, and CO_2 selectivities (red) of the C_3H_6 oxidation with O_2 catalyzed by **a** $c\text{-Cu}_2\text{O-27}$, **b** $c\text{-Cu}_2\text{O-106}$, and **c** $c\text{-Cu}_2\text{O-774}$ NCs. Reaction condition: 200 mg catalyst, 8% C_3H_6 , and 4% O_2 balanced with Ar at a flow rate of 50 mL min^{-1} .

spectroscopic (Supplementary Fig. 8) characterization results show that the structures of spent $c\text{-Cu}_2\text{O-27}$ and $c\text{-Cu}_2\text{O-106}$ NCs at 90 °C and spent $d\text{-Cu}_2\text{O-439}$ at 210 °C are similar to their starting structures, whereas the surfaces of spent $c\text{-Cu}_2\text{O-27}$ and $c\text{-Cu}_2\text{O-106}$ NCs at 150 °C and spent $c\text{-Cu}_2\text{O-774}$ NCs at 210 °C get oxidized, which can be associated with the selective CO_2 production, a highly exothermic reaction. Surface oxidation is more extensive on finer $c\text{-Cu}_2\text{O-27}$ NCs than on $c\text{-Cu}_2\text{O-106}$ NCs. CuO ad-particles on spent $c\text{-Cu}_2\text{O-27}$ and $c\text{-Cu}_2\text{O-106}$ NCs

resulting from surface oxidation were observed to locate preferentially at the edges, supporting that the $\text{Cu}_2\text{O}\{110\}$ edge sites are where the catalytic reactions dominantly occur. In-situ NAP-XPS spectra of $c\text{-Cu}_2\text{O-27}$ NCs under 0.6 mbar $\text{C}_3\text{H}_6 + 0.3$ mbar O_2 (Supplementary Fig. 9) do not show obvious surface oxidation at temperatures up to 150 °C. The discrepancy on surface oxidation of $c\text{-Cu}_2\text{O-27}$ NCs at 150 °C under catalytic reaction and NAP-XPS measurement conditions can be attributed to the existing pressure gap.

Probed by CO adsorption, the oxidation of $\text{Cu}_2\text{O}\{110\}$ edges of *c*- Cu_2O -27 and *c*- Cu_2O -106 NCs at 130 and 150 °C also reduces the available surface Cu(I) sites (Supplementary Fig. 10). We found that C_3H_6 conversion rates of *c*- Cu_2O -27 and *c*- Cu_2O -106 NCs were proportional to the vibrational peak intensities of CO adsorbed at the surface Cu(I) sites at 90 and 130 °C but not at 150 °C (Supplementary Fig. 11). Therefore, the catalytic performances of *c*- Cu_2O -27 and *c*- Cu_2O -106 NCs up to 130 °C are dominantly contributed by the $\text{Cu}_2\text{O}\{110\}$ edges with the Cu(I) sites, and the observed decrease of PO selectivity and increase of CO_2 selectivity at 130 °C should be due to the more extensive over-oxidation of PO. At 150 °C, although less active than the $\text{Cu}_2\text{O}\{110\}$ edge sites, the $\text{Cu}_2\text{O}\{100\}$ face sites of *c*- Cu_2O -27 and *c*- Cu_2O -106 NCs also contribute to the catalytic performance, enhancing the overall CO_2 production and selectivity.

Stability of *c*- Cu_2O -27 NCs at 90 °C was further evaluated. C_3H_6 conversion kept decreasing with the reaction time, while the PO selectivity gradually increased to almost 100% (Supplementary Fig. 12a). XPS spectra show that the surface of spent *c*- Cu_2O -27 NCs is not oxidized (Supplementary Fig. 12b), while C-H species with the C 1s binding energy at 285.4 eV¹² emerges (Supplementary Fig. 12c). Meanwhile, vibration features of carbonate species (1338 and 1537 cm^{-1})²⁹, C-O-C (1046 cm^{-1})³⁰, and C-H ($\sim 2928 \text{ cm}^{-1}$) groups were observed on the spent catalyst (Supplementary Fig. 12d). These observations indicate that oligomers likely form and accumulate to block the active surface sites on *c*- Cu_2O -27 NCs during the catalytic reaction.

Reaction mechanism of C_3H_6 oxidation with O_2 . Figure 3a, b compare C_3H_6 and $\text{C}_3\text{H}_6 + \text{O}_2$ temperature-programmed reaction spectra (TPRS) over *c*- Cu_2O -27 and *d*- Cu_2O -439 NCs. Over *c*- Cu_2O -27 NCs (Fig. 3a), PO ($m/z = 58$ and 31) and CO_2 ($m/z = 44$) productions did not appear in the C_3H_6 -TPRS profile but appeared at ~ 80 °C with similar traces in the $\text{C}_3\text{H}_6 + \text{O}_2$ -TPRS profile. Similar acrolein ($m/z = 56$) production traces

appeared at ~ 100 °C in both C_3H_6 -TPRS and $\text{C}_3\text{H}_6 + \text{O}_2$ -TPRS profiles, and the acrolein production decreased with the temperature increasing in the C_3H_6 -TPRS profile but increased in the $\text{C}_3\text{H}_6 + \text{O}_2$ -TPRS profile. Over *d*- Cu_2O -439 NCs (Fig. 3b), acrolein, PO, and CO_2 productions were observed above 200 °C to display similar traces in the C_3H_6 -TPRS and $\text{C}_3\text{H}_6 + \text{O}_2$ -TPRS profiles with more productions in the presence of O_2 . Thus, no matter at low temperatures over *c*- Cu_2O -27 NCs or at high temperatures over *d*- Cu_2O -439 NCs, the acrolein production by C_3H_6 with O_2 follows the surface lattice oxygen-participated MvK mechanism, consistent with the previous results³¹. The observed decrease of acrolein with the temperature in the C_3H_6 -TPRS profile over *c*- Cu_2O -27 NCs likely arises from the insufficient supply of surface lattice oxygen species at the $\text{Cu}_2\text{O}\{110\}$ edges. The PO production by C_3H_6 with O_2 at high temperatures over *d*- Cu_2O -439 NCs also follows the MvK mechanism, whereas the PO production at low temperatures over *c*- Cu_2O -27 NCs does not, instead, it should follow a LH mechanism involving surface reactions between co-adsorbed propylene and oxygen species. Therefore, propylene epoxidation with O_2 at the $\text{Cu}_2\text{O}\{110\}$ active site follows the LH mechanism at low temperatures and the MvK mechanism at high temperatures.

In-situ DRIFTS measurements of C_3H_6 and $\text{C}_3\text{H}_6 + \text{O}_2$ adsorption on *c*- Cu_2O -27 NCs at different temperatures were carried out to explore the temperature-dependent reaction mechanisms of propylene epoxidation with O_2 (Fig. 3c–e). Assignments of observed vibrational features are summarized in Supplementary Table 2. In addition to gaseous C_3H_6 (2954 and 1652 cm^{-1}), molecularly-adsorbed C_3H_6 species at the Cu(I) site of $\text{Cu}_2\text{O}\{110\}$ edges ($\text{C}_3\text{H}_6(\text{a})_{\text{Cu}}$) (2925 and 1590 cm^{-1}) and bridgingly at Cu(I) and O sites of $\text{Cu}_2\text{O}\{110\}$ edges ($\text{C}_3\text{H}_6(\text{a})_{\text{Cu,O}}$) or bridgingly at O sites of $\text{Cu}_2\text{O}\{100\}$ face sites ($\text{C}_3\text{H}_6(\text{a})_{\text{O,O}}$) (2925 and 1462 cm^{-1}) were observed upon both C_3H_6 and $\text{C}_3\text{H}_6 + \text{O}_2$ adsorption at 25 °C, and all vibrational features disappeared upon evacuation, indicating reversible C_3H_6 adsorption and absence of $\text{C}_3\text{H}_6 + \text{O}_2$ reaction at 25 °C. At 90 °C, C_3H_6

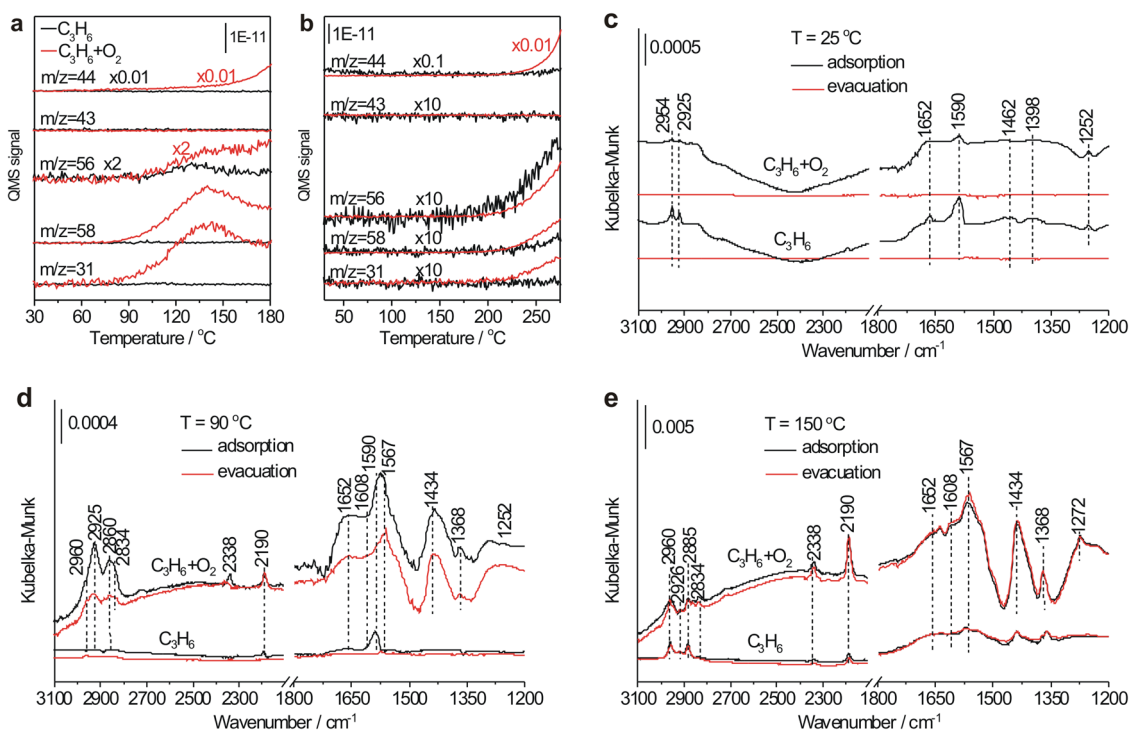


Fig. 3 Reaction mechanism. C_3H_6 -TPRS (8% C_3H_6 in Ar) and $\text{C}_3\text{H}_6 + \text{O}_2$ -TPRS (8% $\text{C}_3\text{H}_6 + 4\% \text{O}_2$ in Ar) of **a** *c*- Cu_2O -27 and **b** *d*- Cu_2O -439 NCs. DRIFTS spectra of C_3H_6 ($P_{\text{C}_3\text{H}_6} = 50 \text{ Pa}$) and $\text{C}_3\text{H}_6 + \text{O}_2$ ($P_{\text{C}_3\text{H}_6} = 50 \text{ Pa}$, $P_{\text{O}_2} = 25 \text{ Pa}$) adsorption on *c*- Cu_2O -27 NCs at **c** 25, **d** 90, and **e** 150 °C.

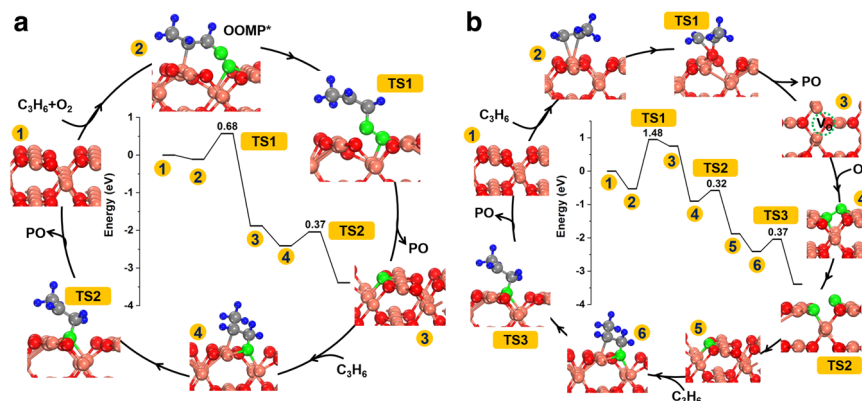


Fig. 4 DFT calculations. Energy profile and catalytic cycle along with the optimized structures of intermediates and transition states for propylene epoxidation on $\text{Cu}_2\text{O}(110)$ via **a** LH and **b** MvK mechanisms. The pink, red, green, gray, and blue spheres represent Cu, O in Cu_2O , O in O_2 , C, and H atoms, respectively.

adsorption dominantly formed $\text{C}_3\text{H}_6(\text{a})_{\text{Cu}}$ species, suggesting that $\text{C}_3\text{H}_6(\text{a})_{\text{Cu}}$ should be more stable than $\text{C}_3\text{H}_6(\text{a})_{\text{Cu},\text{O}}$ and $\text{C}_3\text{H}_6(\text{a})_{\text{O},\text{O}}$, whereas $\text{C}_3\text{H}_6 + \text{O}_2$ adsorption formed not only reversibly-adsorbed C_3H_6 species desorbing upon subsequent evacuation but also surface intermediates remaining upon subsequent evacuation, including $\text{HCOO}(\text{a})$ (2960, 2885, 1567 and 1368 cm^{-1}), allyl adsorbed at the O site ($\text{C}_3\text{H}_5(\text{a})_{\text{O}}$) (2834 and 1608 cm^{-1}), $\text{CO}_2(\text{a})$ (2338 and 2190 cm^{-1}), adsorbed acrolein ($\text{C}_3\text{H}_4\text{O}(\text{a})$) (1652 cm^{-1}), and allyl adsorbed at the Cu site ($\text{C}_3\text{H}_5(\text{a})_{\text{Cu}}$) (1434 cm^{-1}). $\text{HCOO}(\text{a})$ and $\text{CO}_2(\text{a})$ species are the surface intermediates for the CO_2 production, while $\text{C}_3\text{H}_5(\text{a})$ and $\text{C}_3\text{H}_4\text{O}(\text{a})$ species belong to the surface intermediates for the acrolein production. Previous DFT calculation results suggested that the presence of O_2 promoted C_3H_6 dehydrogenation reactions to form adsorbed allyl and acrolein species on Cu_2O surfaces^{32,33}. Therefore, $\text{C}_3\text{H}_6 + \text{O}_2$ adsorption at 90°C involves surface reactions between co-adsorbed $\text{C}_3\text{H}_6(\text{a})$ and oxygen species following the LH mechanism, consistent with the above catalytic performance and TPRS results. Interestingly, few acrolein is produced although $\text{C}_3\text{H}_5(\text{a})$ and $\text{C}_3\text{H}_4\text{O}(\text{a})$ intermediates are formed, whereas PO is the dominant product but few relevant surface intermediates can be identified. This suggests that the desorption of $\text{C}_3\text{H}_4\text{O}(\text{a})$ to produce gaseous acrolein should exhibit a large barrier and barely occur at 90°C , whereas surface reactions producing PO can occur. As the temperature increased to 150°C , the vibrational features of all observed surface intermediates significantly grew, consistent with the enhanced C_3H_6 conversion. Meanwhile, $\text{C}_3\text{H}_6 + \text{O}_2$ adsorption gave the same vibrational bands as C_3H_6 adsorption but with stronger intensities, supporting the above TPRS result that $\text{Cu}_2\text{O}\{110\}$ -catalyzed propylene oxidation with O_2 at high temperatures follows the MvK mechanism. Acrolein production was observed, demonstrating the occurrence of $\text{C}_3\text{H}_4\text{O}(\text{a})$ desorption.

DFT calculations of C_3H_6 oxidation with O_2 . DFT calculations were performed to understand the mechanisms of propylene oxidation at the $\text{Cu}_2\text{O}\{110\}$ active site (Supplementary Table 3). $\text{C}_3\text{H}_6(\text{a})_{\text{Cu}}$ and $\text{C}_3\text{H}_6(\text{a})_{\text{Cu},\text{O}}$ were calculated to exhibit adsorption energy of -0.53 and -0.33 eV and $\text{C}=\text{C}$ stretch vibrational frequency of 1571 and 1444 cm^{-1} , respectively (Supplementary Fig. 13), agreeing with the experimental results. O_2 weakly adsorbs with an adsorption energy of -0.25 eV (Supplementary Fig. 14), and its dissociation into two oxygen adatoms exhibits an enthalpy of -0.12 eV but a barrier of 1.16 eV . It can thus be expected that O_2 dissociation on the perfect $\text{Cu}_2\text{O}\{110\}$ surface is

unlikely at low temperatures. Propylene epoxidation with O_2 at the $\text{Cu}_2\text{O}\{110\}$ active site was found to occur via either a LH mechanism or a MvK mechanism (Fig. 4). The LH mechanism initiates via co-adsorption of C_3H_6 and O_2 to form an oxametallacycle (OOMP) intermediate ($\text{Cu}-\text{O}-\text{O}-\text{CH}_2-\text{CH}(\text{CH}_3)-\text{Cu}$) with a reaction energy of -0.34 eV , which is stronger by 0.26 eV than the formation of $\text{Cu}-\text{O}-\text{O}-(\text{CH}_3)-\text{CH}-\text{CH}_2-\text{Cu}$ intermediate. Then the OOMP intermediate dissociates to produce a PO molecule and an atomic O with a barrier of 0.68 eV . Finally, the resulting atomic O readily reacts with $\text{C}_3\text{H}_6(\text{a})_{\text{Cu}}$ to produce another PO molecule with a barrier of 0.37 eV to close the catalytic cycle of propylene epoxidation with O_2 . Similar mechanisms of C_3H_6 epoxidation with molecularly-adsorbed O_2 species on IB group metal surfaces were proposed by DFT calculations³⁴. The MvK mechanism initiates via the reaction of $\text{C}_3\text{H}_6(\text{a})_{\text{Cu}}$ with surface lattice O to produce a PO molecule and a surface oxygen vacancy (V_O) with a barrier of 1.48 eV . Then O_2 readily dissociates at the V_O site to fill it and produce an atomic O with a barrier of 0.32 eV . Finally, the resulting atomic O readily reacts with $\text{C}_3\text{H}_6(\text{a})_{\text{Cu}}$ to produce another PO molecule with a barrier of 0.37 eV to close the catalytic cycle of propylene epoxidation with O_2 .

Propylene partial oxidation to acrolein at the $\text{Cu}_2\text{O}\{110\}$ active site following the MvK mechanism was also calculated (Supplementary Fig. 15). It initiates by an abstract of an α -H atom of $\text{C}_3\text{H}_6(\text{a})_{\text{Cu}}$ to produce $\text{C}_3\text{H}_5(\text{a})_{\text{Cu}}$ or $\text{C}_3\text{H}_5(\text{a})_{\text{O}}$ with a barrier of 0.75 eV . The $\text{C}_3\text{H}_5(\text{a})_{\text{O}}$ is more stable than the $\text{C}_3\text{H}_5(\text{a})_{\text{Cu}}$ species by 0.90 eV , resulting in a larger barrier of the $\text{C}_3\text{H}_5(\text{a})_{\text{O}}$ -to- $\text{C}_3\text{H}_4\text{O}(\text{a})$ reaction (1.77 eV) than of the $\text{C}_3\text{H}_5(\text{a})_{\text{Cu}}$ -to- $\text{C}_3\text{H}_4\text{O}(\text{a})$ reaction (1.05 eV). Then the resulting $\text{C}_3\text{H}_4\text{O}(\text{a})$ species desorbs to produce an acrolein molecule and create a surface oxygen vacancy with a barrier of 0.96 eV . The H-abstraction reactions of $\text{C}_3\text{H}_6(\text{a})_{\text{Cu}}$ to produce $\text{C}_3\text{H}_4\text{O}(\text{a})$ were previously calculated to be promoted by co-adsorbed O_2 species, but the $\text{C}_3\text{H}_4\text{O}(\text{a})$ desorption still exhibited a barrier of 0.99 eV ³². Meanwhile, the $\text{C}=\text{C}$ bond breaking of $\text{C}_3\text{H}_6(\text{a})_{\text{O},\text{O}}$ on the $\text{Cu}_2\text{O}\{100\}$ surface by surface lattice oxygen to eventually produce CO_2 was previously calculated with a barrier of 1.05 eV ¹⁷.

The above DFT calculation results suggest that the largest barrier is 0.68 eV among elementary surface reactions of LH mechanism for $\text{Cu}_2\text{O}\{110\}$ -catalyzed propylene epoxidation, but is 0.99 – 1.77 eV of MvK mechanism for $\text{Cu}_2\text{O}\{110\}$ -catalyzed propylene epoxidation, LH and MvK mechanisms for $\text{Cu}_2\text{O}\{110\}$ -catalyzed propylene partial oxidation to acrolein, and MvK mechanism for $\text{Cu}_2\text{O}\{100\}$ -catalyzed propylene combustion. Meanwhile, due to the very small adsorption energy but very large dissociation barrier of $\text{O}_2(\text{a})$, $\text{O}_2(\text{a})$ is the dominant

adsorbed oxygen species on the stoichiometric $\text{Cu}_2\text{O}\{110\}$ site and can only form at low temperatures. Thus, at low temperatures at which $\text{O}_2(\text{a})$ forms, $\text{Cu}_2\text{O}\{110\}$ -catalyzed propylene epoxidation following the LH mechanism occurs and other reactions with large barriers barely, leading to the high PO selectivity; however, at high temperatures at which $\text{O}_2(\text{a})$ is few, $\text{Cu}_2\text{O}\{110\}$ -catalyzed propylene epoxidation following the LH mechanism barely occurs although with low barriers, and $\text{Cu}_2\text{O}\{110\}$ -catalyzed propylene epoxidation and propylene partial oxidation to acrolein and $\text{Cu}_2\text{O}\{100\}$ -catalyzed propylene combustion, all following the MvK mechanism, occur to produce PO, acrolein and CO_2 , respectively. These DFT calculation results agree well with the experimental observations of temperature-dependent catalytic selectivity of our fine $c\text{-Cu}_2\text{O}$ NCs in propylene oxidation with O_2 . Thus, the reactivity and temperature-dependent coverages of various surface species at different surface sites of Cu_2O NCs are responsible for the observed apparent catalytic activity and selectivity in propylene oxidation with O_2 .

Discussion

In summary, based on the fundamental understanding of the active site of Cu_2O catalysts for propylene epoxidation with O_2 , we successfully explore finely-sized cubic Cu_2O NCs with a high density of active $\text{Cu}_2\text{O}\{110\}$ edge sites as the highly selective catalyst to catalyze propylene epoxidation with O_2 . Over the $c\text{-Cu}_2\text{O}$ -27 NCs catalyst, $\text{Cu}_2\text{O}\{110\}$ -catalyzed propylene epoxidation with weakly adsorbed $\text{O}_2(\text{a})$ species as the active oxygen species exhibits a low barrier and is the dominant reaction occurring at low temperatures, selectively producing PO with a selectivity of above 80%, whereas $\text{Cu}_2\text{O}\{110\}$ -catalyzed propylene partial oxidation and propylene epoxidation and $\text{Cu}_2\text{O}\{100\}$ -catalyzed propylene combustion, all with surface lattice oxygen as the dominant active oxygen species and exhibiting large barriers, occur at high reaction temperatures, producing acrolein, PO and CO_2 , respectively. These results demonstrate the effectiveness of fundamental understanding in guiding the exploration of efficient catalysts for challenging heterogeneous catalytic reactions.

Methods

Chemicals and materials. All chemical reagents with the analytical grade were purchased from Sinopharm Chemical Reagent Co. C_3H_6 (99.95%), O_2 (99.999%), CO (99.99%), and Ar (99.999%) were purchased from Nanjing Shangyuan Industrial Factory. All chemicals were used as received.

Synthesis of $c\text{-Cu}_2\text{O}$ -27 and $c\text{-Cu}_2\text{O}$ -106 NCs. $c\text{-Cu}_2\text{O}$ -27 and $c\text{-Cu}_2\text{O}$ -106 NCs were synthesized according to the method reported by Chang et al.²⁶. To synthesize $c\text{-Cu}_2\text{O}$ -27 NCs, 1 mL CuSO_4 aqueous solution (1.2 mol L^{-1}) was rapidly injected into 400 mL deionized water at 25°C . After stirring for 5 min, 1 mL NaOH aqueous solution (4.8 mol L^{-1}) was poured into the solution. After stirring for another 5 min, 1 mL ascorbic acid aqueous solution (1.2 mol L^{-1}) was injected. Then the solution was kept for another 30 min, and the resulting precipitate was collected by centrifugation, decanting, and washing with distilled water and absolute ethanol, and finally dried in vacuum at RT for 12 h. $c\text{-Cu}_2\text{O}$ -106 NCs were synthesized similarly, except that 0.26 g sodium citrate was added to the initial 400 mL deionized water at 25°C .

Synthesis of $c\text{-Cu}_2\text{O}$ -774 NCs. $c\text{-Cu}_2\text{O}$ -774 NCs were synthesized according to the following typical procedure²⁵. 5.0 mL NaOH aqueous solution (2.0 mol L^{-1}) was added dropwise into 50 mL CuCl_2 aqueous solution (0.01 mol L^{-1}) at 60°C . After adequately stirring for 0.5 h, 5.0 mL ascorbic acid aqueous solution (0.6 mol L^{-1}) was added dropwise into the solution. The mixed solution was adequately stirred at 60°C for 5 h. The resulting precipitate was collected by centrifugation, decanting, and washing with distilled water and absolute ethanol, and finally dried in vacuum at RT for 12 h.

Synthesis of $d\text{-Cu}_2\text{O}$ -439 NCs. $d\text{-Cu}_2\text{O}$ -439 NCs capped with oleic acid (OA) (denoted as $d\text{-Cu}_2\text{O}$ -439-OA) were synthesized following Liang et al.'s procedure²⁷. Typically, under vigorous stirring, 4 mL OA was mixed with 20 mL of absolute ethanol, and slowly added to 40 mL CuSO_4 aqueous solution (0.025 mol L^{-1}). The

mixture was heated to 100°C for 0.5 h. Then 10 mL NaOH aqueous solution (0.8 mol L^{-1}) was added. After stirring for another 5 min, 30 mL $D\text{-}(+)\text{-glucose}$ aqueous solution (0.63 mol L^{-1}) was quickly added. The obtained mixture was stirred at 100°C for another 1 h, and its color changed from black to green, and finally to brick red. The resulting precipitate was collected by centrifugation, decanting, and washing with distilled water and absolute ethanol, and finally dried in vacuum at RT for 12 h.

Capping ligands on as-synthesized $d\text{-Cu}_2\text{O}$ -439-OA NCs were removed following Hua et al.'s procedure¹⁷. Typically, 150 mg $d\text{-Cu}_2\text{O}$ -439-OA NCs were placed in a U-shaped quartz microreactor and purged in the stream of $\text{C}_3\text{H}_6 + \text{O}_2 + \text{Ar}$ gas mixture (C_3H_6 : O_2 : $\text{Ar} = 2:1:22$) with a flow rate of 50 mL min^{-1} at RT for 0.5 h, and then heated to 215°C at a heating rate of 5°C min^{-1} and kept for another 0.5 h. Then the sample was cooled down to room temperature to acquire $d\text{-Cu}_2\text{O}$ -439 NCs.

In-situ C_3H_6 and $\text{C}_3\text{H}_6 + \text{O}_2$ DRIFTS. Diffuse reflectance infrared spectroscopy (DRIFTS) measurements of chemisorption processes were performed on a Nicolet 6700 FTIR spectrometer equipped with an in-situ DRIFTS reaction cell (Harrick Scientific Products, INC) and a MCT/A detector. 50 mg catalyst was loaded onto the sample stage of the reaction cell. Prior to the experiments, the sample was heated at the desired temperatures at pressures better than 0.1 Pa, and the spectrum was measured and used as the background spectrum, then the adsorbed gas was admitted into the reaction cell to desirable pressures through a leak valve, and the DRIFTS spectra were recorded after the chemisorption processes reached a steady state.

In-situ $\text{C}_3\text{H}_6 + \text{O}_2$ NAPXPS. Near-ambient pressure X-ray photoelectron spectroscopy (NAPXPS) measurements were carried out at BL02B01 of Shanghai Synchrotron Radiation Facility³⁵. The bending magnet beamline delivered a soft X-ray with photon flux around 1×10^{11} photons s^{-1} , energy resolution of $E/\Delta E = 3700$ and beam spot size of $\sim 200 \mu\text{m} \times 75 \mu\text{m}$ on the sample. XPS spectra were calibrated using $\text{Au } 4f_{7/2}$ binding energy at 84.0 eV. During the NAPXPS experiments, 0.6 mbar C_3H_6 and 0.3 mbar O_2 were introduced into the chamber, and the $c\text{-Cu}_2\text{O}$ NCs were heated and stabilized at desirable temperatures for 0.5 h, and then the NAPXPS spectra were measured.

Structural characterizations. Power X-ray diffraction (XRD) patterns were conducted on a Philips X'Pert PROS diffractometer using a nickel-filtered $\text{Cu K}\alpha$ (wavelength: 0.15418 nm) radiation source with the operation voltage and operation current being 50 mA and 40 kV, respectively. X-ray photoelectron spectroscopy (XPS) was carried out on an ESCALAB 250 high-performance electron spectrometer using monochromatized $\text{Al K}\alpha$ ($h\nu = 1486.7 \text{ eV}$) as the excitation source. The likely charging of samples was corrected by setting the binding energy of the adventitious carbon ($\text{C } 1s$) to 284.8 eV. Scanning electron microscope (SEM) images were obtained on a JEOL JSM-6700 field emission scanning electron microscope. Transmission electron microscopy (TEM), high-resolution transmission electron microscopy (HRTEM) were obtained on a JEM-2100F high-resolution transmission electron microscope.

C_3H_6 -temperature-programmed reaction spectra (C_3H_6 -TPRS) and $\text{C}_3\text{H}_6 + \text{O}_2$ TPRS were measured in a quartz tube microreactor equipped with an axial quartz sheathed thermocouple and connected to an online mass spectrometer (HIDEN QIC-20). In the C_3H_6 -TPRS experiments, 50 mg catalyst was pretreated in Ar with a flow rate of 30 mL min^{-1} at 200°C for 0.5 h and then cooled to 30°C , then the gas stream was switched to 8% C_3H_6 in Ar with a flow rate of 50 mL min^{-1} and the catalyst was heated at a heating rate of 5°C min^{-1} . In the $\text{C}_3\text{H}_6 + \text{O}_2$ TPRS experiments, 50 mg catalyst was pretreated in Ar with a flow rate of 30 mL min^{-1} at 200°C for 0.5 h and then cooled to 30°C , then the gas stream was switched to 8% $\text{C}_3\text{H}_6 + 4\% \text{ O}_2$ in Ar with a flow rate of 50 mL min^{-1} and the catalyst was heated to the desired temperature at a heating rate of 5°C min^{-1} .

In-situ CO adsorption after catalytic reactions at different temperatures was performed on a Nicolet 6700 FTIR spectrometer equipped with an in-situ low-temperature and vacuum DRIFTS reaction cell (Harrick Scientific Products, Inc.) in order to enhance the chemisorption with minimum interference of gas-phase molecules. The DRIFTS spectra were measured with 256 scans and a resolution of 4 cm^{-1} using a MCT/A detector. 50 mg catalyst was loaded on the sample stage of the reaction cell. Prior to adsorption experiments, the sample was evacuated at 293 K for 1 h at a base pressure of 0.1 Pa and then cooled to 123 K, whose spectrum was taken as the background spectra. Then CO was admitted into the reaction cell to the desirable pressures via a leak valve, and the DRIFTS spectrum was recorded after the chemisorption reached the steady state.

Catalytic performance evaluation. Catalytic performance of Cu_2O nanocrystals in propylene oxidation with O_2 without any pretreatments was evaluated in a quartz tube microreactor equipped with an axial quartz sheathed thermocouple. 200 mg catalyst was used and heated to the desired reaction temperatures at a rate of 2°C min^{-1} in a reaction gas mixture (C_3H_6 : O_2 : $\text{Ar} = 2:1:22$, flow rate: 50 mL min^{-1}). After the catalytic reaction reached a steady state, the composition of outlet gas was analyzed using an online Shimadzu GC-2014 gas chromatograph equipped with two flame ionization detectors (FIDs) and one thermal conductivity

detector (TCD). One FID was attached to a Stabilwax-DA capillary column (0.53 mm × 60 m) to detect propylene and oxygenates (acetaldehyde, PO, acetone, propionaldehyde, acrolein, acetic acid, and isopropanol) to a detection limit of 1 ppm, and the TCD was attached to a Porapak Q (3 mm × 3 m) and C13x compact column (3 mm × 3 m, Shimadzu) to detect O₂. A CH₄ conversion oven was connected to the end of the TCD to convert trace CO₂ to CH₄, whose concentration was detected by the other FID. All the lines and valves between the exit of the reactor and the gas chromatographs were heated to 80 °C to prevent condensation of the products. The activity and selectivity of the catalytic reaction were calculated as the following, in which X_i represents conversion, S_i selectivity, m_i mass, and n_i moles of substance i, FC_{3H6} represents the flow rate of C₃H₆:

$$X_{C_3H_6} = \frac{n_{\text{oxygenates}} + n_{CO_2/3}}{n_{\text{propyleneinfeed}}} \quad (1)$$

$$S_{PO} = \frac{n_{PO}}{n_{\text{oxygenates}} + n_{CO_2/3}} \quad (2)$$

$$S_{\text{Acrolein}} = \frac{n_{\text{Acrolein}}}{n_{\text{oxygenates}} + n_{CO_2/3}} \quad (3)$$

$$S_{CO_2} = \frac{n_{CO_2/3}}{n_{\text{oxygenates}} + n_{CO_2/3}} \quad (4)$$

$$C_3H_6 \text{ reaction rate} = \frac{X_{C_3H_6} \times FC_{C_3H_6}}{m_{\text{catalyst}}} \quad (5)$$

DFT calculations. DFT calculations were performed by Vienna ab initio Simulation Package (VASP)^{36,37}. The exchange–correlation interaction was described by the Bayesian error estimation functional with van der Waals correlation (BEEF–vdW)³⁸. The Kohn–Sham equations were solved by a plane wave basis set with a kinetic energy cutoff of 400 eV. A Cu₂O(110) surface with (2 × 2) unit cell was modeled by a slab model including four-layer O and seven-layer Cu atoms. To prevent the artificial interaction between the repeated slabs along z-direction, 15 Å vacuum was introduced with correction of the dipole moment. The (2 × 2 × 1) k-point mesh was used to sample the Brillouin zone. During the optimization, the bottom two-layer O and four-layer Cu atoms were fixed in their bulk positions, while the remained atoms and adsorbates were relaxed until the residual forces were less than 0.02 eV Å⁻¹. DFT + U correction was used with U–J = 6 eV for Cu 3d-orbitals³⁹. Adsorption energies were calculated by E_{ads} = E_{ad/sub} – E_{ad} – E_{sub}, where E_{ad/sub}, E_{ad}, and E_{sub} were the total energies of the optimized adsorbate/substrate system, the adsorbate in the gas phase, and the clean substrate, respectively. Transition states of the elementary steps were located by the climbing-image nudged elastic band (CI-NEB) method⁴⁰.

Data availability

The data supporting the findings of the study are available within the paper and its Supplementary Information. Source data are provided with this paper.

Received: 29 May 2021; Accepted: 21 September 2021;

Published online: 11 October 2021

References

- Myers, R. L. *The 100 Most Important Chemical Compounds* (Greenwood Press, London, 2007).
- Nijhuis, T. A., Makkee, M., Moulijn, J. A. & Weckhuysen, B. M. The production of propene oxide: Catalytic processes and recent developments. *Ind. Eng. Chem. Res.* **45**, 3447–3459 (2006).
- Russo, V., Tesser, R., Santacesaria, E. & Di Serio, M. Chemical and technical aspects of propene oxide production via hydrogen peroxide (HPPO Process). *Ind. Eng. Chem. Res.* **52**, 1168–1178 (2013).
- Leow, W. R. et al. Chloride-mediated selective electrosynthesis of ethylene and propylene oxides at high current density. *Science* **368**, 1228–1233 (2020).
- Huang, J. & Haruta, M. Gas-phase propene epoxidation over coinage metal catalysts. *Res. Chem. Intermed.* **38**, 1–24 (2011).
- Khatib, S. J. & Oyama, S. T. Direct oxidation of propylene to propylene oxide with molecular oxygen: a review. *Catal. Rev. Sci. Eng.* **57**, 306–344 (2015).
- Teržan, J., Huš, M., Likozar, B. & Djinić, P. Propylene epoxidation using molecular oxygen over copper- and silver-based catalysts: a review. *ACS Catal.* **10**, 13415–13436 (2020).
- Lei, Y. et al. Increased silver activity for direct propylene epoxidation via subnanometer size effects. *Science* **328**, 224–228 (2010).
- Zhan, C. et al. Critical roles of doping Cl on Cu₂O nanocrystals for direct epoxidation of propylene by molecular oxygen. *J. Am. Chem. Soc.* **142**, 14134–14141 (2020).
- Marimuthu, A., Zhang, J. & Linic, S. Tuning selectivity in propylene epoxidation by plasmon mediated photo-switching of Cu oxidation state. *Science* **339**, 1590–1593 (2013).
- He, J., Zhai, Q., Zhang, Q., Deng, W. & Wang, Y. Active site and reaction mechanism for the epoxidation of propylene by oxygen over CuO_x/SiO₂ catalysts with and without Cs⁺ modification. *J. Catal.* **299**, 53–66 (2013).
- Yang, X. et al. Direct epoxidation of propylene over stabilized Cu⁺ surface sites on titanium-modified Cu₂O. *Angew. Chem. Int. Ed.* **54**, 11946–11951 (2015).
- Zhu, W., Zhang, Q. & Wang, Y. Cu(I)-catalyzed epoxidation of propylene by molecular oxygen. *J. Phys. Chem. C* **112**, 7731–7734 (2008).
- Vaughan, O., Kyriakou, G., Macleod, N., Tikhov, M. & Lambert, R. Copper as a selective catalyst for the epoxidation of propene. *J. Catal.* **236**, 401–404 (2005).
- Wang, Y., Chu, H., Zhu, W. & Zhang, Q. Copper-based efficient catalysts for propylene epoxidation by molecular oxygen. *Catal. Today* **131**, 496–504 (2008).
- Su, W., Wang, S., Ying, P., Feng, Z. & Li, C. A molecular insight into propylene epoxidation on Cu/SiO₂ catalysts using O₂ as oxidant. *J. Catal.* **268**, 165–174 (2009).
- Hua, Q. et al. Crystal-plane-controlled selectivity of Cu₂O catalysts in propylene oxidation with molecular oxygen. *Angew. Chem. Int. Ed.* **53**, 4856–4861 (2014).
- Torres, D., Lopez, N., Illas, F. & Lambert, R. M. Why copper is intrinsically more selective than silver in alkene epoxidation: ethylene oxidation on Cu(111) versus Ag(111). *J. Am. Chem. Soc.* **127**, 10774–10775 (2005).
- Besenbacher, F. et al. Design of a surface alloy catalyst for steam reforming. *Science* **279**, 1913–1915 (1998).
- Nørskov, J. K., Bligaard, T., Rossmeisl, J. & Christensen, C. H. Towards the computational design of solid catalysts. *Nat. Chem.* **1**, 37–46 (2009).
- Seh, Z. W. et al. Combining theory and experiment in electrocatalysis: Insights into materials design. *Science* **355**, eaad4998 (2017).
- Studt, F. et al. Discovery of a Ni-Ga catalyst for carbon dioxide reduction to methanol. *Nat. Chem.* **6**, 320–324 (2014).
- Honkala, K. et al. Ammonia synthesis from first-principles calculations. *Science* **307**, 555–558 (2005).
- Zhang, Z. et al. Site-resolved Cu₂O catalysis in the oxidation of CO. *Angew. Chem. Int. Ed.* **58**, 4276–4280 (2019).
- Zhang, D.-F. et al. Delicate control of crystallographic facet-oriented Cu₂O nanocrystals and the correlated adsorption ability. *J. Mater. Chem.* **19**, 5220–5225 (2009).
- Chang, I. C. et al. Large-scale synthesis of uniform Cu₂O nanocubes with tunable sizes by in-situ nucleation. *CrystEngComm* **15**, 2363–2366 (2013).
- Liang, X., Gao, L., Yang, S. & Sun, J. Facile synthesis and shape evolution of single-crystal cuprous oxide. *Adv. Mater.* **21**, 2068–2071 (2009).
- Huang, W. Oxide nanocrystal model catalysts. *Acc. Chem. Res.* **49**, 520–527 (2016).
- Chen, S. et al. Probing surface structures of CeO₂, TiO₂, and Cu₂O nanocrystals with CO and CO₂ chemisorption. *J. Phys. Chem. C* **120**, 21472–21485 (2016).
- Yang, P. F., Li, J. Y. & Li, T. D. Characterization on propylene oxide polymerization with in situ FT-IR. *Adv. Mater. Res.* **160–162**, 60–64 (2010).
- Reitz, J. B. & Solomon, E. I. Propylene oxidation on copper oxide surfaces: electronic and geometric contributions to reactivity and selectivity. *J. Am. Chem. Soc.* **120**, 11467–11478 (1998).
- Xiao, T.-T., Li, R.-S. & Wang, G.-C. A DFT study and microkinetic simulation in propylene oxidation on the “29” Cu_xO/Cu(111) surface. *J. Phys. Chem. C* **124**, 6611–6623 (2020).
- Song, Y. Y. & Wang, G. C. Theoretical study of propylene epoxidation over Cu₂O(111) surface: activity of O²⁻, O⁻, and O₂⁻ species. *J. Phys. Chem. C* **122**, 21500–21513 (2018).
- Dai, Y. et al. Significant enhancement of the selectivity of propylene epoxidation for propylene oxide: a molecular oxygen mechanism. *Phys. Chem. Chem. Phys.* **19**, 25129–25139 (2017).
- Cai, J. et al. An APXPS endstation for gas–solid and liquid–solid interface studies at SSRF. *Nucl. Sci. Tech.* **30**, 81 (2019).
- Kresse, G. & Furthmüller, J. Efficient iterative schemes for ab initio total-energy calculations using a plane-wave basis set. *Phys. Rev. B* **54**, 11169–11186 (1996).
- Kresse, G. & Furthmüller, J. Efficiency of ab-initio total energy calculations for metals and semiconductors using a plane-wave basis set. *Comput. Mater. Sci.* **6**, 15–50 (1996).
- Wellendorff, J. et al. Density functionals for surface science: exchange–correlation model development with Bayesian error estimation. *Phys. Rev. B* **85**, 235149 (2012).
- Isseroff, L. Y. & Carter, E. A. Importance of reference Hamiltonians containing exact exchange for accurate one-shot GW calculations of Cu₂O. *Phys. Rev. B* **85**, 235142 (2012).
- Henkelman, G., Uberuaga, B. P. & Jonsson, H. A climbing image nudged elastic band method for finding saddle points and minimum energy paths. *J. Chem. Phys.* **113**, 9901–9904 (2000).

Acknowledgements

This work was financially supported by the National Natural Science Foundation of China (91945301, 21525313, 91745202), the Chinese Academy of Sciences, and the Changjiang Scholars Program of the Ministry of Education of China. The DFT calculations were performed on the supercomputing center of Wuhan University. The NAP-XPS measurements were carried out at the beamline 02B01 of the Shanghai Synchrotron Radiation Facility supported by the National Natural Science Foundation of China under contract no. 11227902.

Author contributions

W.X. carried out the experiments. X.-K.G. carried out the DFT calculations. Z.Z., P.C., Y.Z., Z.Y., D.L., H.Z., and Z.L. assisted with the experiments. W.H. designed and supervised the project. All authors analyzed the data. W.H., W.X., and X.-K.G. prepared the manuscript and other authors commented on the manuscript.

Competing interests

The authors declare no competing interests.

Additional information

Supplementary information The online version contains supplementary material available at <https://doi.org/10.1038/s41467-021-26257-0>.

Correspondence and requests for materials should be addressed to Weixin Huang.

Peer review information *Nature Communications* thanks Petar Djinović and the other, anonymous, reviewers for their contribution to the peer review of this work. Peer reviewer reports are available.

Reprints and permission information is available at <http://www.nature.com/reprints>

Publisher's note Springer Nature remains neutral with regard to jurisdictional claims in published maps and institutional affiliations.



Open Access This article is licensed under a Creative Commons Attribution 4.0 International License, which permits use, sharing, adaptation, distribution and reproduction in any medium or format, as long as you give appropriate credit to the original author(s) and the source, provide a link to the Creative Commons license, and indicate if changes were made. The images or other third party material in this article are included in the article's Creative Commons license, unless indicated otherwise in a credit line to the material. If material is not included in the article's Creative Commons license and your intended use is not permitted by statutory regulation or exceeds the permitted use, you will need to obtain permission directly from the copyright holder. To view a copy of this license, visit <http://creativecommons.org/licenses/by/4.0/>.

© The Author(s) 2021, corrected publication 2021